JGR Earth Surface

RESEARCH ARTICLE
10.1029/2022JF006817

Special Section:
Fire in the Earth System

Transient Freeze-Thaw Deformation Responses to the 2018 and 2019 Fires Near Batagaika Megaslump, Northeast Siberia

K. Yanagiya[1,2], M. Furuya[3,4], P. Danilov[5], and G. Iwahana[4,6]

[1]Graduate School of Science, Hokkaido University, Sapporo, Japan, [2]Now at Earth Observation Research Center, Japan Aerospace Exploration Agency, Tsukuba, Japan, [3]Faculty of Science, Hokkaido University, Sapporo, Japan, [4]Arctic Research Center, Hokkaido University, Sapporo, Japan, [5]Institute of Northern Applied Ecology, North-Eastern Federal University in Yakutsk, Yakutsk, Russia, [6]International Arctic Research Center, University of Alaska Fairbanks, Fairbanks, AK, USA

Key Points:

- Transient post-fire deformations at the 2018 and two 2019 scars near Batagay were examined by satellite radar and onsite thaw depth data
- The northern 2019 scar subsided by 13 cm in the first span-fire year, but the other two scars uplifted and started to subside during the next year
- The duration of frost heave is longer in the next year after fire than in the burned year because of more soil water in the active layer

Supporting Information:

Supporting Information may be found in the online version of this article.

Correspondence to:

K. Yanagiya and M. Furuya,
yanagiya.kazuki@jaxa.jp;
furuya@sci.hokudai.ac.jp

Citation:

Yanagiya, K., Furuya, M., Danilov, P., & Iwahana, G. (2023). Transient freeze-thaw deformation responses to the 2018 and 2019 fires near Batagaika megaslump, Northeast Siberia. *Journal of Geophysical Research: Earth Surface*, *128*, e2022JF006817. https://doi.org/10.1029/2022JF006817

Received 1 JUL 2022
Accepted 27 JAN 2023

Author Contributions:

Conceptualization: M. Furuya
Data curation: K. Yanagiya
Formal analysis: K. Yanagiya, G. Iwahana
Funding acquisition: M. Furuya, G. Iwahana
Investigation: K. Yanagiya, P. Danilov, G. Iwahana

Abstract Wildfires in Arctic regions impact landforms via permafrost degradation and subsequent deformation that can last for many years. However, it remains uncertain on if and how much deformations occur, and what controls their magnitude, particularly during the first couple of years. Here, we examine the transient post-fire deformation responses near the Batagaika megaslump, which is the world's largest retrogressive thaw slump at Batagay, Sakha Republic. There were wildfires in the summers of 2018 and 2019 on the same slope, which could trigger the formation of another megaslump; many fires occurred nearby in 2019. We use interferometric synthetic aperture radar (InSAR) to measure surface displacements, including both post-fire and span-fire images. We also perform onsite measurements of temperature and thaw depth around the two scars near Batagaika megaslump in 2019, 2020, and 2021 and around the 2014 scar in 2019. At the three fire scars formed in 2018 and 2019, we demonstrate year-to-year and location-specific changes in the amplitude of subsidence, heave, and duration. The 2018 scar shows cumulative subsidences of up to 10 cm by March 2021, more clearly than the nearby 2019 scar. On the other hand, another 2019 scar adjacent to the 2014 scar shows up to 13 cm net subsidence during the first span-fire year, although the subsiding area is limited. These diverse transient post-fire responses demonstrate that under the yedoma area the spatial heterogeneities of the active layer depth and the timing of fires will control subsequent thermokarst processes.

Plain Language Summary Wildfires in Arctic regions impact landforms via permafrost degradation and subsequent deformation that can last for many years. However, it remains uncertain on if and how much post-fire deformation has been taking place, and what controls the magnitude of ground deformation is unclear, especially in the first couple of years after the fire. Here, we examine the transient post-fire responses to the three fire scars formed in 2018 and 2019 near Batagay, Northeast Siberia. Two of the fires occurred on the same slope as the "Batagaika crater," the world's largest surface depression initiated by deforestation in the 1970s. We used not only the satellite-based imaging tool called Interferometric Synthetic Aperture Radar (InSAR) to detect the surface deformation signals but also onsite measurements to detect the spatial-temporal depth changes of the active layer. The inferred transient post-fire responses are rather diverse despite the shared climate, suggesting that the prefire depth to the permafrost table will play the most crucial role in controlling the subsequent subsidence.

1. Introduction

Wildfire in the Arctic region is responsible for deepening active layer thickness (ALT), defined as the maximum annual thaw depth (e.g., Yoshikawa et al., 2003; Zhang et al., 2015). Moreover, when the underlying permafrost is either ice-rich or includes massive ground ice, it can further change the local terrains, known as thermokarst, because either thawing of the permafrost table or melting of massive ice will lead to irreversible ground subsidence if meltwater drains away (Holloway et al., 2020; Jorgenson, 2013; Kokelj & Jorgenson, 2013). These impacts by wildfire are not only because thermal insulation effects of vegetation cover are lost but also because the subsequent increase in soil water content (SWC) and albedo reduction can assist permafrost thaw and ice melting (e.g., Yoshikawa et al., 2003; Zhang et al., 2015). Furthermore, it takes several years for the vegetation to recover, so ALT deepening and permafrost thaw can last for years (Frost et al., 2020). Still, the details of how the permafrost landscape responds to fires remain uncertain.

Methodology: M. Furuya, P. Danilov, G. Iwahana
Project Administration: M. Furuya
Resources: P. Danilov
Software: K. Yanagiya
Supervision: M. Furuya, G. Iwahana
Validation: K. Yanagiya, P. Danilov, G. Iwahana
Visualization: K. Yanagiya
Writing – original draft: K. Yanagiya, M. Furuya
Writing – review & editing: M. Furuya, G. Iwahana

Meanwhile, the number of fires and burned areas are increasing in the Arctic region in recent decades (Gillett et al., 2004; Kasischke et al., 2010; McCarty et al., 2021; Ponomarev et al., 2016), and thus they could further accelerate ALT deepening and permafrost degradation. Moreover, as permafrost in high-latitude regions stores twice as much carbon as in the atmosphere, its thawing can enhance microbial decomposition of organic carbon and result in greenhouse gas emissions, such as CO_2 and CH_4, known as permafrost carbon feedback (Schuur et al., 2015; Tarnocai et al., 2009; Turetsky et al., 2020). Therefore, it is essential to quantitatively evaluate how the active layer and permafrost will respond to fires.

ALT changes after fires have been well documented based on field-based thaw probe measurements (e.g., Yoshikawa et al., 2003). Recent studies have estimated them by measuring surface displacements using satellite-based InSAR data (e.g., Liu, Jafarov, et al., 2014; Michaelides et al., 2019; Molan et al., 2018; Schaefer et al., 2015). InSAR also allows us to evaluate the impact of wildfires on thermokarst processes (Iwahana et al., 2016; Yanagiya & Furuya, 2020). However, the loss of interferometric coherence often limits the availability of useful InSAR data to interpret the permafrost dynamics, particularly before and after fires, due to the dramatic changes in the microwave scattering characteristics (Liu, Jafarov, et al., 2014; Molan et al., 2018). As a result, all previous deformation mapping at fire scars has used either prefire or only post-fire images, and the transient responses to wildfires remain obscured. For instance, it has been uncertain from InSAR data alone if ALT deepening and permafrost thaw occur in the burned year before the freezing season or the following year after initiating the next thawing season. Nonetheless, in the previous models of post-fire deformation (Michaelides et al., 2019; Molan et al., 2018), they assumed that the InSAR-derived deformation between two epochs is a combination of the linear secular term and seasonal term; the former represents permafrost thaw subsidence, and the latter can be estimated by Stefan equation from accumulated degree days of thawing/freezing (ADDT/ADDF). Liu, Jafarov, et al. (2014) did not include the linear term because of the short temporal coverage but set the factors for seasonal terms different between prefire and post-fire periods. The model was originally proposed by Liu et al. (2010) to interpret the 8-year' InSAR data over the North Slope of Alaska unrelated to fires. However, it is not evident if we can similarly apply the model to post-fire responses; Liu et al. (2015) applied this model to thermokarst subsidence triggered by the construction of pipeline access roads in the 1970s. During the early post-fire phase, in particular, we expect transient changes in the subsidence rate and the amplitude of ALT deepening that will also depend on when the fire takes place. Moreover, the uplift signal (frost heave) was assumed to be due to volume expansion of pore water into ice by phase change over the freezing depth estimated from the Stefan equation (Liu et al., 2012; Molan et al., 2018). However, frost heave is widely known to be caused by ice lens formation by water migration from below Taber (1929, 1930) and Gruber (2020) showed significant differences in the observed subsidence and heave from the predictions by the Stefan equation.

Here, we also use InSAR data to examine the transient post-fire displacements, which are the first couple of years after fire, at the three fire scars near Batagaika megaslump (BMS). The three fire scars are all within 30 km distance from each other but differ, at least, in terms of the timing, duration, and location of the fires. We give a brief description of the site and the details of the 2018 and 2019 fires in the next section. As in our previous work on the 2014 fire near Batagay (Figure 1a), we used two types of InSAR data derived from C-band Sentinel-1B and L-band ALOS-2 (Yanagiya & Furuya, 2020). Because of its shorter recurrent period of 12 days, Sentinel-1B InSAR data can tell the surface deformation with higher temporal resolution. On the other hand, L-band ALOS-2 InSAR data have better temporal coherence than C-band and allow us to examine 1-year cumulative displacements using two images acquired, for instance, in March and the following March. However, it is not always possible to generate a 1-year interferogram depending on the status of the scattering surfaces. We can also take advantage of the dry snow in the study area, which maintains good coherence even in winter. We can thus isolate transient, non-cyclic, and span-fire freeze-thaw deformation responses over 1 year. The post-fire seasonal changes will no longer be cyclic, particularly during the first couple of years.

This study aims to demonstrate and interpret the transient freeze-thaw deformation responses at the three fire scars under a common climate. It turns out that there are a variety of transient freeze/thaw deformation responses, depending on each fire scar. We discuss our interpretations of the differences in the subsidence/uplift amplitude and implications for the impact of wildfires on thermokarst processes. We also discuss the possibility of another megaslump formation based on InSAR data and our preliminary onsite observations.

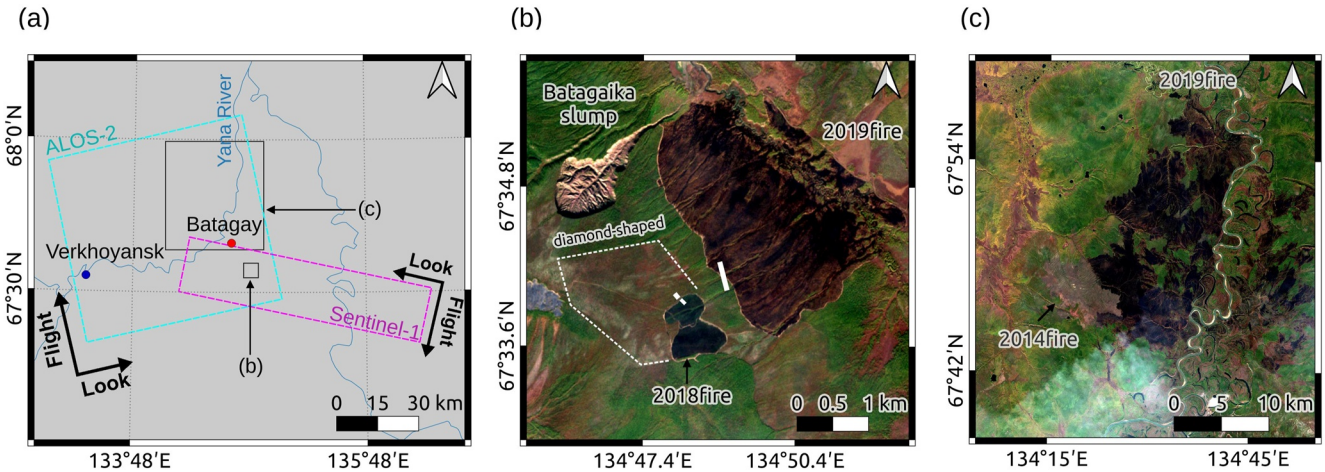

Figure 1. (a) Map around Batagay. Cyan and magenta dashed-boxes indicate the imaging areas of ALOS-2 and the clipped Sentinel-1, respectively. Also shown are the locations of panels (b and c). (b) Wildfire scars located very close to the Batagaika megaslump from Sentinel-2 image on 31 August 2019. The small-western scar was burned in 2018, and the large-eastern scar was burned in 2019. White points and lines are the in situ observation sites in 2019, 2020, and 2021; the expanded view is shown in Figure 2a. There is also one less-vegetated "diamond-shaped" area immediately to the northwest of the 2018 scar. (c) Wildfire scars located to the north of Batagay across the Yana river; note that the scale is different from (b). The large 2019 scar is located to the east of the 2014 scar reported by Yanagiya and Furuya (2020).

2. Study Site

Batagay (67°39′30″N, 134°38′40″E) is located on the Yana River, which is 872 km long and covers a 238,000 km^2 basin in a part of the East Siberian Lowlands in the Sakha Republic (Figure 1a). The climate is highly continental with mean annual air temperature of −12.4°C and mean annual precipitation 203 mm during 1988–2017 (Kizyakov et al., 2023; Murton et al., 2022). The presence of the BMS has been attracting a good deal

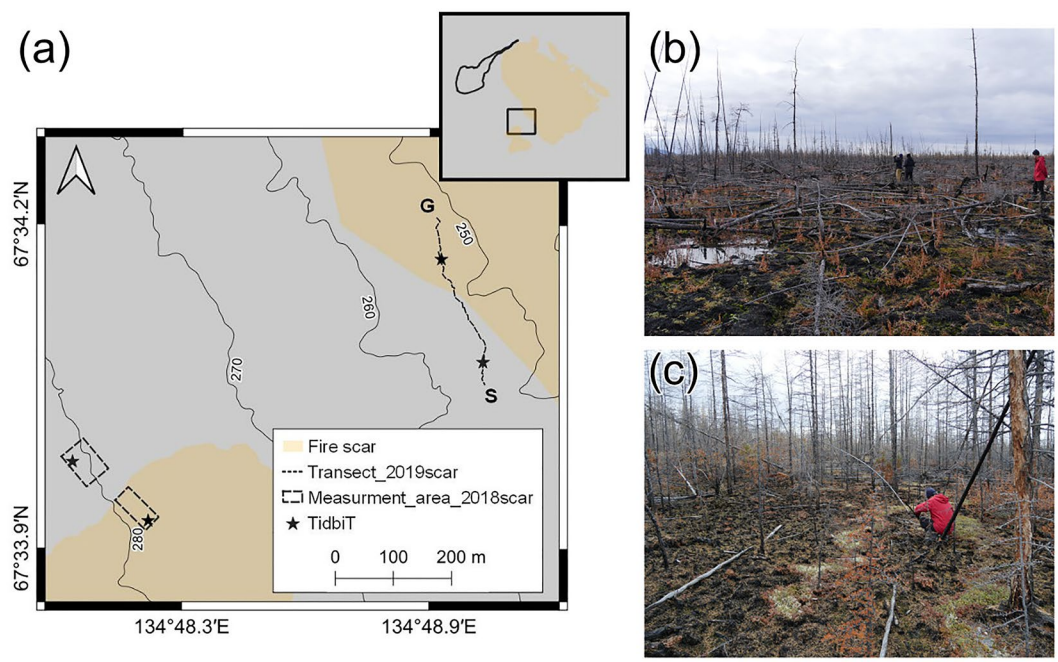

Figure 2. (a) The map of field observation area near Batagaika megaslump (BMS). Orange areas are the 2018 and 2019 fire scars, black dashed squares inside and outside the 2018 scar indicate the thaw depth measurement areas, and the black dashed line, G-S, indicates the transect near the boundary of the 2019 fire scar. Black stars indicate the location of TidbiT loggers for temperature time series. (b) Sample photo of the 2018 fire scar taken on 23 September 2019. (c) Sample photo of the 2019 fire scar taken on September 23, 2019.

of cryological and geomorphological attention because it is the world's largest retrogressive thaw slump, located 12 km southeast of Batagay village (Figure 1b). BMS exposes roughly 50–90 m thick yedoma deposits on the north-east facing slope (e.g., Kizyakov et al., 2023; Kunitsky et al., 2013); yedoma is a unique permafrost deposit in terms of its high volume of ice (50%–90%) and organic-rich sediments. BMS itself provides us not only a window into the past climate due to the exposed ancient permafrost but also a natural laboratory to examine how permafrost thaw proceeds during the present Arctic warming (Kizyakov et al., 2023).

Unlike the previous studies on post-fire deformation response with InSAR (e.g., Liu, Jafarov, et al., 2014; Liu, Schaefer, et al., 2014; Michaelides et al., 2019; Molan et al., 2018), our study site is in the yedoma area, where we expect an irreversible subsidence once the ground ice are melted. Furthermore, the thaw subsidence due to the melt of thick ice lenses often seen in the transient layer (uppermost permafrost layer) is not fully recoverable by a single winter freeze. Those thick lenses develop during multi-year aggradation of permafrost (Shur et al., 2005).

Our focus in this study is not on the BMS itself but on the deformation responses to the three fires near the BMS. Two of them were formed in 2018 and 2019 and are located adjacent to the BMS. Another one was burned in 2019 and is located northwest of the Yana River and adjacent to the 2014 scar where Yanagiya and Furuya (2020) reported the post-fire deformation (Figure 1c).

The 2018 and 2019 fires near BMS were from August 4 to 6 in 2018 and from July 12 to July 23 in 2019, respectively (Sentinel-2, NASA FIRMS [https://firms.modaps.eosdis.nasa.gov/map/]). Both scars are on the same slope as BMS (Figure 1b), whose mean dip angle is 2° toward the northeast, and the slope becomes nearly flat near the Batagay river. As the formation of BMS was initiated by deforestation and subsequent erosion on a small gully in the 1970s (Kunitsky et al., 2013), the nearby wildfires could trigger the formation of another megaslump. It is thus vital to keep monitoring if and how the topography will change after the fires. The duration of another 2019 fire adjacent to the 2014 scar to the northwest (Figure 1c) is June 9 to 26 (FIRMS), which means 1 month and 2 months longer than the two scars above in terms of the positive degree days and thus may promote permafrost thawing more efficiently. Computing the delta normalized burn ratio from Sentinel-2 images, the burn severities of the three scars are roughly identical, while there are some spatial heterogeneities within the two 2019 fires (Figure S1 in Supporting Information S1).

At the 2018 and 2019 scars near the BMS, we show year-to-year changes in the amplitude and duration of frost-heave signals and non-cyclic net annual subsidences. Moreover, although it is outside the scars, one less-vegetated "diamond-shaped" area near the two fire scars (Figure 1b) shows a frost heave signal but differs from the two scars in amplitude and duration. This area will also help interpret the permafrost distribution of the site in combination with thaw depth data. At another northern 2019 scar adjacent to the 2014 scar (Figure 1c), the span-fire InSAR data during the first year show greater subsidence signals, as detailed in Section 4.4. The greater subsidence is consistent with the adjacent 2014 scar.

3. Data and Methods

3.1. InSAR Data

InSAR is a space geodetic technique to detect the relative ground deformation in the imaged area as phase changes between two imaging periods (see Bürgmann et al., 2000; Massonnet & Feigl, 1998; Simons & Rosen, 2015); the reference pixels are assumed to be stable over the periods. InSAR is thus insensitive to spatially homogenous ground deformation known as "isotropic thaw subsidence" (Shiklomanov et al., 2013) whose spatial scale is greater than that covered by SAR images. We used the GAMMA software, version 20200728 (Wegmüller & Werner, 1997), to generate differential interferograms for each satellite data. The DEM data used to remove the topographic phase was ArcticDEM 10 m mosaic (Porter et al., 2018), which is fine enough for the spatial resolution of the present InSAR images. Also, we used QGIS version 3.10.8 to stack the interferograms and generate deformation maps. Although "stacking" has often been used to generate an average deformation rate map by reducing tropospheric noise, here we intend to simply combine each interferogram to generate cumulative LOS changes over a certain period. Except for the early summer season, we could always generate InSAR images with the shortest temporal baseline. Also, as we have clipped the analysis area, we can virtually ignore the atmospheric errors (e.g., Hanssen, 2001) by polynomial fitting and do not have to rely on the so-called time-series analysis technique.

InSAR image contains long-wavelength signals due to troposphere (e.g., Goldstein, 1995) and ionosphere (e.g., Gomba et al., 2016) in addition to ground deformation signals. To reduce atmospheric signals, we fit all the

phase-unwrapped InSAR images with a quadratic polynomial and subtracted the calculated trend. After removing the long-wavelength trend, the phase change is close to zero outside the fire scars except for the "diamond-shaped" area noted below.

Details of ALOS-2 and Sentinel-1 data in this study are shown in Table S1 and S2 of Supporting Information S1; ALOS-2 and Sentinel-1 are used to examine long-term and seasonal changes, respectively, because few ALOS-2 summer data are available, and Sentinel-1 loses coherence for long-term pairs. ALOS-2 and Sentinel-1 data for the two fire scars near BMS and the northern 2019 scar are acquired at the same track (Table S1 and S2 in Supporting Information S1). Regardless of either ALOS-2 or Sentinel-1, a low coherence problem arises due to the changes in scattering properties and/or processes such as the ground surface scattering to volume scattering within the snow layer (Tsai et al., 2019). The coherence loss is severe for pairs with snowmelt water in summer and wet snow in winter. Likewise, early-summer and late-summer data lose coherence, probably due to the differences in the surface wetness. For dry snow, however, Rignot et al. (2001) reported that microwaves could penetrate the snow layer several meters, and a satellite could receive backscatter from the ground surface. Dry snow does not cause a coherence loss but can generate a frequency-dependent phase delay due to changes in snow water equivalent (SWE) (Guneriussen et al., 2001). Since we remove the long-wavelength trend, we can ignore the effect of spatially uniform changes in SWE. Although there are no independent observations to support the dry snow assumption, Yanagiya and Furuya (2020) confirmed that the displacements obtained from winter pairs with nearly the same period were consistent in both L-band and C-band InSAR images at the 2014 fire scar, 15 km northwest of Batagay.

InSAR data is a projection of the actual 3D displacements onto the radar Line-Of-Sight (LOS) direction. Now, the ALOS-2 illuminates the surface from west to east with 38.0 degrees of incidence angle, whereas the Sentinel-1 does from east to west with 38.7 degrees of incidence angle (Figure 1a); InSAR data are most sensitive to the vertical displacement and insensitive to the north-south displacement because of the near-polar orbit. We stacked several Sentinel-1 InSAR images to match the measurement interval to the ALOS-2 InSAR images and compared the seasonal deformations. Despite the different illumination directions of both satellites, the derived InSAR LOS changes in both satellites are consistent in terms of the spatial pattern and only different below ~1 cm (Figure S2 in Supporting Information S1), which indicates the dominance of vertical displacements in the LOS changes, as confirmed in the 2014 scar as well (Yanagiya & Furuya, 2020). Yet, all the LOS changes below are not projected to the vertical to keep the original data.

3.2. Thaw Depth and Temperature Data

We measured thaw depths by inserting a metal probe at the 2018 and 2019 scars near the BMS at the end of the summer season when they become the deepest in a year. We performed the first measurement on 23 September 2019, the second on 12 September 2020, and the third on 17 September 2021. Figure S7 in Supporting Information S1 indicates that the temperature dropped below zero in early October. Hence, the thaw depth data below can be regarded as ALT. Figure 2a shows the detailed location of the measurement sites. Unfortunately, we could not access the northern 2019 scar because of its remoteness and limited time. However, at the time of onsite measurements in 2019, we collected the thaw depth data at the 2014 scar that are helpful for comparison (Figure S3 in Supporting Information S1).

At the 2018 scar (Figure 2b), we randomly measured thaw depths at 50, 20, and 30 points in about 70×30 m^2 area in 2019, 2020, and 2021, respectively (Figure 2a). In addition, a control site was set at the adjacent unburned area, where we measured the same number of points as those at the burned area in about 70×50 m^2 area each year. The control site for the 2018 scar is actually inside the "diamond-shaped area" (Figure 1b) that is less vegetated but exhibits some anomalous displacements, as shown below.

At the 2019 scar (Figure 2c), we set up a straight 300 m transect that starts from the unburned control site (S) and ends inside the scar (G; Figure 2a) and measured thaw depths along with the transect. The measurements were performed at 53 points in the fire scar and 59 points in the control site in 2019. During onsite surveys in 2020 and 2021, we measured again but with fewer points due to the limited time at 27 points in the fire scar and 30 points in the control site, respectively.

In addition, we installed TidbiT thermometers in the 2018 and 2019 scars and adjacent unburned areas (Figure 2a) to help interpret the thermal regime changes. The thermometers logged hourly raw data from 24 September 2019, and we collected them on 16 September 2021. We installed them at two types of places; one is attached to a larch

tree shaded by bark fragments at the height of about 180 cm to measure air temperature, and the other is on the surface to measure surface temperature. More precisely, they are on the organic layers in unburned areas and on the mineral ground or mineral layer in burned areas. Unfortunately, we could not retrieve all the air temperature data because of the attack by woodpeckers on larch and accidental failure during the collection.

4. Results

4.1. Seasonal Frost Heave Immediately After Fires Near Batagaika Megaslump

Figure 3 shows seasonal frost heave maps near BMS during early, mid, and late winter in 2018, 2019, and 2020, derived by stacking Sentinel-1 InSAR images; the division into the three winter sub-phases is based on the heave signals by InSAR. We compare the seasonal frost heave signals during the 3 years; the original 12-day interval InSAR images are shown in Figures S4–S6 of Supporting Information S1; some pixels are missing due to phase unwrapping error due to low coherence.

Early winter covers from mid-September to early November when the air temperature drops below the freezing point and frost heave starts (Figure S7 in Supporting Information S1). The impact of wildfire during early winter is observed as frost heave by ∼6 cm uplift in both Figures 3a and 3d for the 2018 and 2019 scars, respectively. Besides the scars, we can point out clear uplift at the diamond-shaped area outside the 2018 scar that repeats every year but occurs only in the early winter (Figures 3a, 3d, and 3g). Moreover, the heaving duration in the diamond-shaped area is shorter than in the scars (Figures S4–S6 in Supporting Information S1). The Sentinel-2 image indicates that the diamond-shaped area is less vegetated (Figure 1b) and probably indicates a former deforested area; it is uncertain when precisely the deforestation was done. Smaller uplift signals by up to 2 cm at the 2019 scar were also observed in 2018 (Figure 3a), which we can confirm with both Sentinel-1 and ALOS-2 InSAR data over the low-elevation area (Figure S2 in Supporting Information S1); Figure S2 in Supporting Information S1 indicates that the uncertainty is 1 cm at 2-sigma level. No significant uplift at the exact low-elevation location occurred after the 2019 fire as shown in Figures 3d–3i.

Mid-winter covers from November to December when the air temperature drops below −20°C (Figure S7 in Supporting Information S1). No significant uplift signals were found outside the scars, including the diamond-shaped area (Figures 3b, 3e, and 3h). At the 2018 scar, although Figure 3b shows no significant uplift, Figures 3e and 3h indicate that frost heave is lasting. We can confirm the extended heave duration at the 2019 scar as well in light of Figures 3e and 3h, except for the low-elevation portion of the 2019 scar. Namely, the heave duration is extended in the second year after the fire. The seasonal changes in the surface temperature data do not show any significant differences in 2019 and 2020 (Figure S7 in Supporting Information S1), indicating that the surface temperature does not cause the extended heave duration.

Late winter covers from December to April, and the surface temperature is still below freezing (Figure S7 in Supporting Information S1). Figures 3c, 3f, and 3i show no clear signals, suggesting that the thawed layer during the summer was entirely frozen by late winter.

4.2. Net Annual Ground Deformation at the Fire Scars Near Batagaika Megaslump

Figures 4a–4c are ALOS-2 InSAR images covering 1 year from March 2018, 2019, and 2020, respectively. In previous studies, an InSAR image, when it includes a fire period, has lost interferometric coherence between primary and secondary images, and no span-fire deformation data were available (e.g., Liu, Jafarov, et al., 2014; Molan et al., 2018). However, in the study area, the coherence of the 1-year InSAR image with March data is high enough to tell the net annual deformation signal even when the fire period is included between the two epochs; the coherence with the June data is worse (Figure S8 in Supporting Information S1). Assuming that secular subsidence signals are much smaller than the seasonal subsidence and uplift, the 1-year InSAR images help examine the transient processes toward a new normal state because the former normal seasonal processes below the surface vegetation are disrupted by fire.

Figures 4a and 4b show excess uplift by up to 1 and 3 cm at the 2018 and 2019 scars, respectively, during the one span-fire year between prefire March and post-fire March. A closer look into Sentinel-1 data indicates that the subsidence lasting for 2 weeks after the 2018 fire (Figures S4k and S4l in Supporting Information S1) is reversed by subsequent uplift by frost heave (Figures S4m–S4o in Supporting Information S1). We also confirm the early

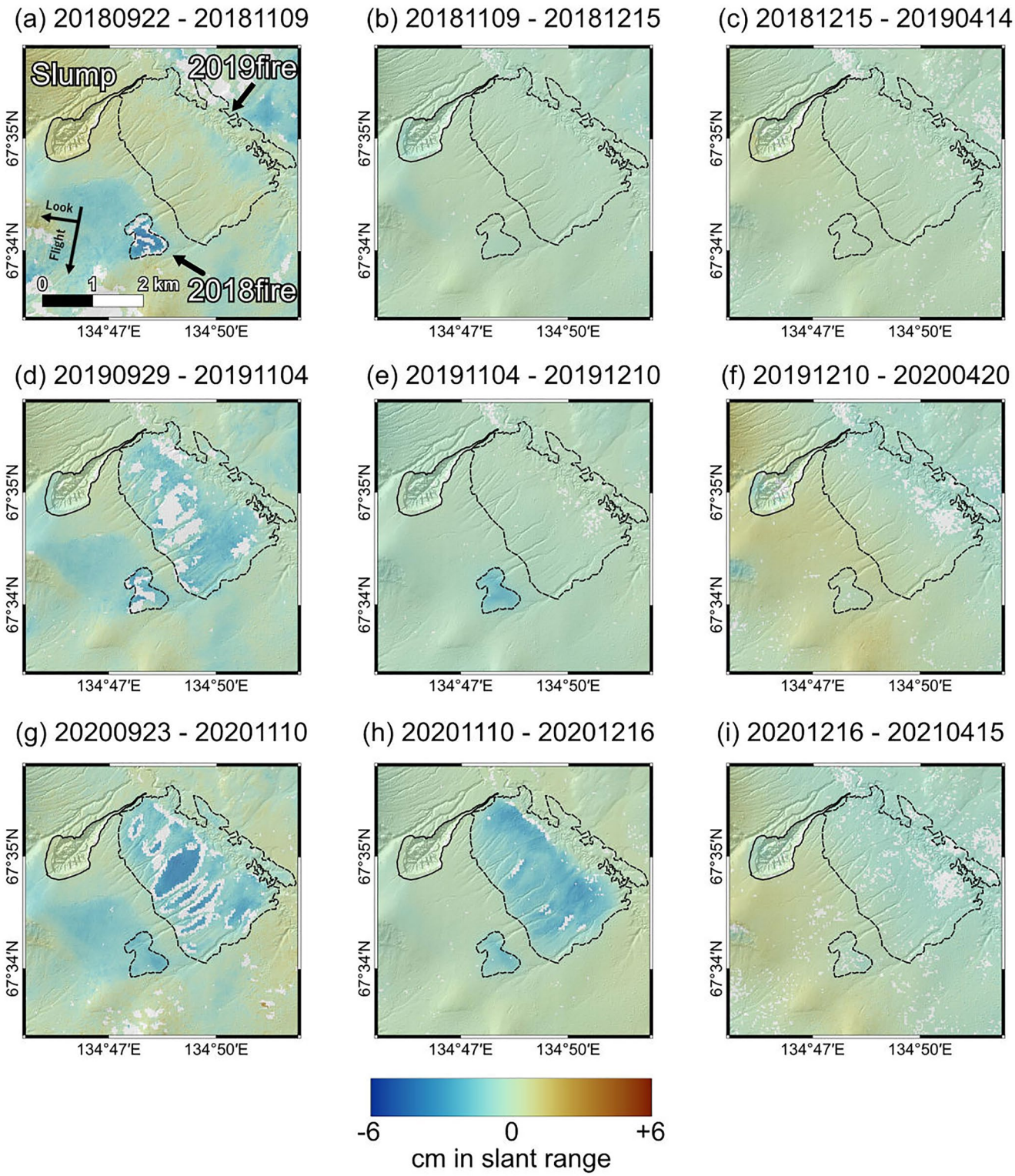

Figure 3. Frost heave maps derived from stacked Sentinel-1 InSAR images (from yyyymmdd to yyyymmdd). See Table S2 and Figures S4–S6 in Supporting Information S1 for the original data. The left (a,d,g), central (b,e,h), and right (c,f,i) columns are early, mid, and late winter, respectively. Warm and cold colors indicate the subsidence and uplift in the LOS direction, respectively. The black line is the Batagaika megaslump derived from the Sentinel-2 optical image in 21 June 2020. The west and east black dashed lines are the fire scars burned in 2018 and 2019, respectively. The background is shaded-relief computed from the DEM.

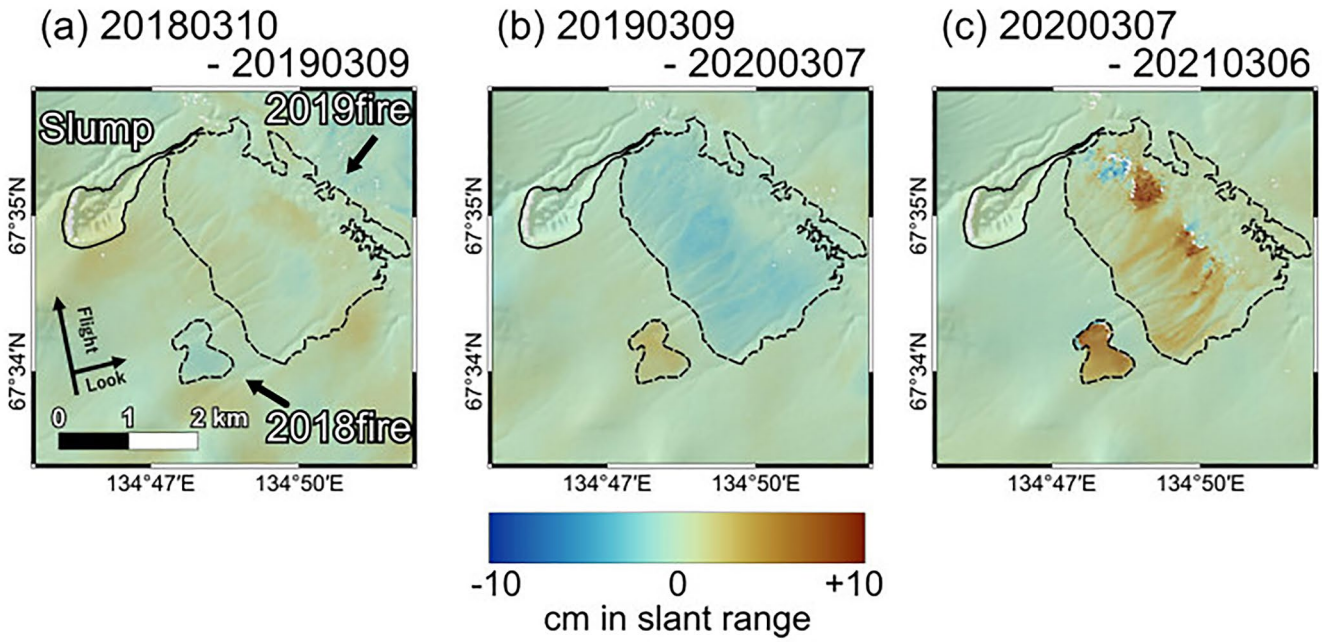

Figure 4. ALOS-2 InSAR images covering 1 year (from yyyymmdd to yyyymmdd). Panels (a–c) are total LOS changes starting from March 2018, 2019, and 2020, respectively. LOS changes toward the satellite, meaning an uplift, are detected in the 2018 and 2019 scars in the burned year. Phase unwrapping errors cause some discontinuous phase changes in (c). The background is shaded-relief computed from the DEM.

subsidence and subsequent excess uplift at the 2019 fire scar (Figures S5j, S5m, and S5n in Supporting Information S1). Figure 4 also shows that the net annual subsidence starts the following year after the fire; however, this is not the case at another 2019 scar to the north, as shown in subsection 4.4. At the 2018 scar, Figures 4b and 4c indicate that the annual subsidence in 2020 is even larger than in 2019. At the 2019 fire scar, on the other hand, the yearly subsidence is smaller than at the 2018 scar and spatially more heterogeneous than at the 2018 fire scar (Figure 4c); the discontinuous changes in Figure 4c are most likely due to unwrapping errors.

Besides the clear net annual signals at the scars, we realize the absence of such signals at the diamond-shaped area to the west of the 2018 scar, where seasonal uplift signals clearly show up in Figures 3a, 3d, and 3g. We will discuss our interpretations later on.

4.3. Seasonal Frost Heave Immediately After the Fire to the North of Batagay

Figure 5 shows seasonal frost heave maps at the 2019 scar to the north, which is located immediately to the east of the 2014 scar (Figure 5a). While the decorrelation problem keeps from showing heave signals in the first early winter at the 2019 scar (Figure 5a and Figure S9 in Supporting Information S1), the winter Sentinel-1 interferograms have higher coherence than the summer pairs and show uplift signals from late winter in 2019 (Figures 5b, 5d, and 5e); however, we could not clearly detect seasonal subsidence (Figures S9 and S10 in Supporting Information S1). While the uplift amounts are small by as much as ∼1 cm in mid-winter 2019 (Figure 5b), those in early and mid-winter 2020 became larger by up to ∼6 cm (Figures 5d and 5e). Namely, the heave duration extended in the second year after the fire, similar to the near-slump scars (Figure 3).

The topography-correlated signals in Figures 5c and 5f indicate tropospheric phase delay that could not be corrected by low-order polynomials because the area coverage is more extensive than in Figures 3 and 4. No differences across the boundary of the fire scars suggest that the thawed layer is frozen entirely, as shown in Figures 3 and 4.

4.4. Net Annual Ground Deformation at the 2019 Fire Scar to the North

Figures 6a and 6b are span-fire 1-year ALOS-2 InSAR images from January 2019 and March 2019, respectively. Despite the 2-month differences in their acquisition dates, both images are nearly identical in terms of spatial distribution and amplitude of the LOS changes. The localized span-fire LOS changes indicate significant subsidence signals by 13 cm at maximum. They are unlikely to be apparent deformation signals due to tropospheric

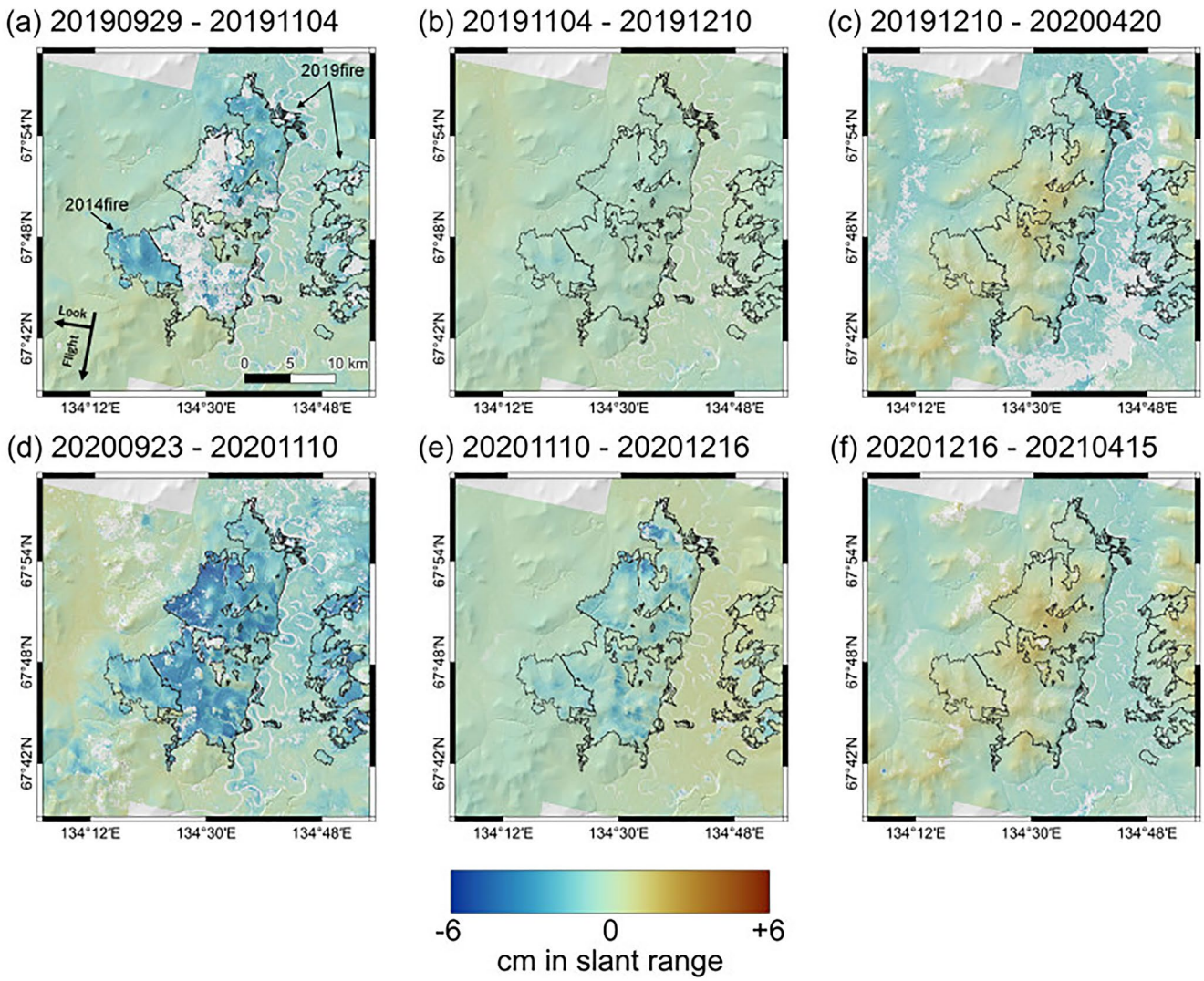

Figure 5. Frost heave maps derived from stacked Sentinel-1 InSAR images (from yyyymmdd to yyyymmdd). The left (a and d), central (b and e), and right (c and f) columns are early, mid, and late winter, respectively. The black dashed lines indicate the 2014 and 2019 fire scars to the north. The background is shaded-relief computed from the DEM. The elevation difference from the highest peak to the flank is ~340 m.

delays because they should distribute randomly in space and time. Another possible source of artifact deformation signals is SWE. Still, there would be no reason why the SWE is anomalously large in those areas because of no correlations with local topography and slope aspect. Figure 6c is the first post-fire 1-year ALOS-2 InSAR image from March 2020 and indicates the increase in the subsidence amplitude and the expansion of the subsidence area.

The annual subsiding areas were heterogeneous compared to the seasonal heave areas (Figure 5d) and were rather significant in the western regions close to the 2014 scar. Unlike the 2014 scar (Yanagiya & Furuya, 2020), however, there is no systematic trend in the subsiding area regarding slope aspect and topography. Also, the subsidence pattern is not correlated with the burn severity, whose spatial pattern is almost uniform in the fire scars (Figure S1 in Supporting Information S1). Considering the uplift signals derived from Sentinel-1 data (Figure 5), the subsiding signals probably exceed the uplifting signal to generate the net annual subsidence in Figure 6.

4.5. Thaw Depth Changes

Figures 7a and 7b summarize the thaw depth data at the 2018 and 2019 scars with those at the nearby controlled areas, respectively, derived just before the winter season. In 2019, the mean thaw depth at the 2018 scar was about 103 ± 19 cm (Figure 7a), deeper by more than 60 cm than at the nearby unburned area, where the mean thaw depth is 43 ± 15 cm. In 2020, the thaw depth at the 2018 scar deepened further and reached 134 ± 23 cm

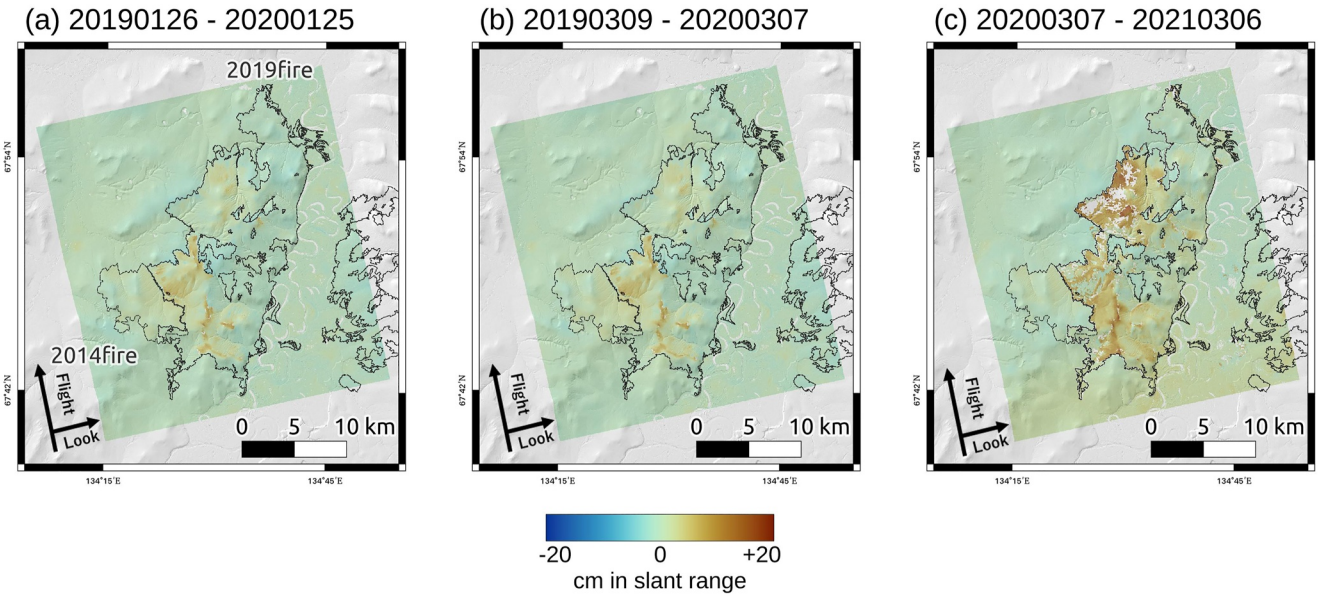

Figure 6. (a), (b) ALOS-2 InSAR images covering one span-fire year (from yyyymmdd to yyyymmdd) starting from January 2019 to March 2019, respectively. (c) ALOS-2 InSAR image for the first post-fire year. LOS changes away from the satellite, meaning subsidence, are detected in the southwestern part of the 2019 scar in the burned year. The thin and thick black dashed lines indicate the 2014 and 2019 scars, respectively. Note that the range of the color scale is larger than that in Figure 4. The background is shaded-relief computed from the DEM.

in 2021, while the deepening rate slowed down. On the other hand, the mean thaw depths inside and outside the 2019 scar were 78 ± 25 cm and 66 ± 29 cm in 2019 (Figure 7b), indicating that they are slightly deeper inside the scar but are not significantly different; see also Figure 7c. The 2019 scar deepened in 2020 and reached about 132 ± 11 cm depth in 2021 (Figure 7b). The thaw depth at the 2019 scar control site was originally about 20 cm deeper than that at the control site for the 2018 scar (Figure 7). The thaw depths have indeed deepened by the 2018 and 2019 fires, but it is uncertain when the ALT deepening was initiated, which would depend on both the original prefire thaw depth and the timing of the fire.

Figure 7c indicates the thaw depths measured along the transect from point S to point G in the 2019 scar (Figure 2a). The unburned area covers from the point U010 to U300, showing mostly stable thaw depths over the 3 years. Thaw depth deepens at point U300 since the point is located on an excavated road with no surface organic layer, forming a boundary between unburned and burned sites. The burned area is from point B010 to B270. The thaw depths increased rapidly at all the points in 2020 and continued to deepen in 2021, with a few exceptions.

The shallower thaw depth adjacent to the 2018 scar was derived from the diamond-shaped area (Figure 1b), where we could observe clear seasonal frost heave in Figure 3 without net annual subsidence in Figure 4. We will discuss its implications below.

5. Discussion

5.1. Limitations of Stefan Function Approach for Seasonal Deformation Modeling

The thawing/freezing depth (Z) of soil can be estimated using the Stefan function (Nelson et al., 1997):

$$Z(t) = \sqrt{\frac{2knA(t)}{\rho\theta L}}$$

where k is soil thermal conductivity, n is the n-factor defined as the ratio of ground surface temperature and air temperature, $A(t)$ is ADDT or ADDF for either thawing or freezing season with t denoting the SAR data acquisition date, θ is the volumetric water content; ρ is the bulk soil density, and L is the latent heat of fusion for water (Klene et al., 2001; Liu et al., 2012). The Stefan function is helpful to evaluate thawing/freezing depth when only air or ground surface temperature data are available. In contrast, the thermal conductivity, n-factor, and volumetric water content are largely uncertain, site-specific, and time-variable after surface disturbances.

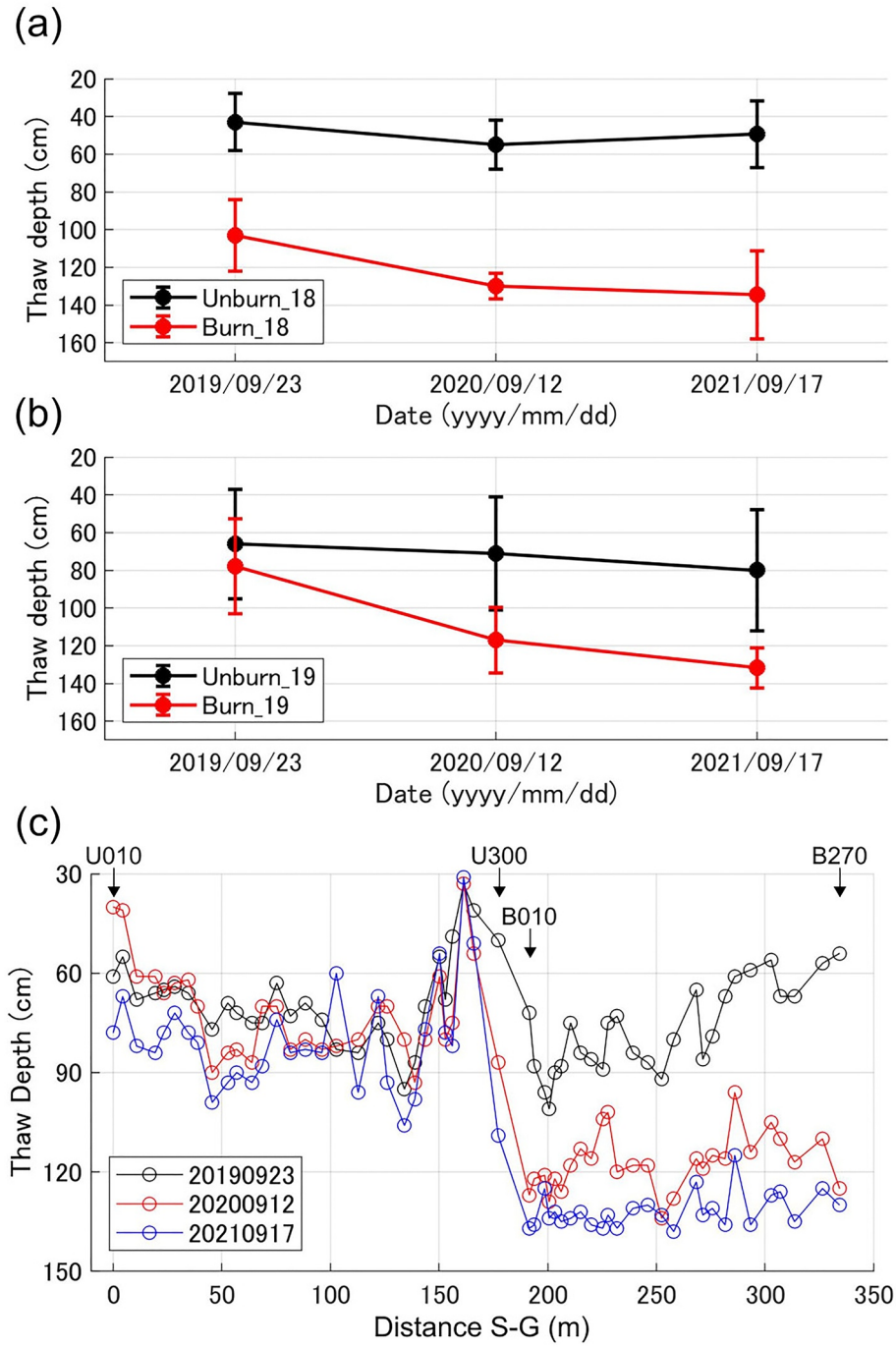

Figure 7. (a) Temporal changes in mean thaw depth at the 2018 scar. The black and red lines represent mean values taken at unburned and burned sites, respectively. Error bars indicate the estimated standard deviation with 2σ. (b) Temporal change of mean thaw depth at the 2019 scar. (c) The original thaw depth profiles along the transect S-G in Figure 2a and their temporal changes before averaging. The unburned site near the 2019 scar is from point U010 to U300. The burned site inside the 2019 scar is from point B010 to B270. The black, red, and blue lines indicate thaw depth at each measurement point in 2019, 2020, and 2021, respectively.

To predict the amplitude of seasonal thaw subsidence/uplift, one needs to further assume physical processes for thawing/freezing. Liu et al. (2012) and Hu et al. (2018) assumed that the volume expansion by phase change of soil pore water into ice over the thaw depth was responsible for the uplift. Following this phase change model under the assumption of fully water-saturated soil, we would expect greater uplift where the freezing depth is deeper;

Figure 8. Photo of an on-site pit inside the "diamond-shaped" area as the control site of 2018 scar, taken on 18 September 2021. There was an ice lens at the bottom of the pit, which is significantly shallower than the 2019 controlled site (Figure 7).

likewise, greater summer subsidence would be expected from a deeper thaw depth. However, despite the shallower thaw depth at the diamond-shaped area (Figure 7a) overlapping the 2018 controlled site, we have observed greater seasonal subsidence and frost-heave signals (Figures S5 and S6 in Supporting Information S1) but no net annual subsidences (Figures 3 and 4). Given our onsite observations at a pit inside the diamond-shaped area (Figure 8), the ground surface is covered by the organic layer's mat with ∼10 cm thickness, but the soils are well wet, demonstrating very high SWC. The observed shallower thaw depth thus presumably indicates that the permafrost table was originally closer to the surface than at the 2019 controlled site. Despite the shallower thaw depth, the organic layers seem to have prevented the near-surface permafrost from extensive thawing thus little net subsidence. On the other hand, the shallower thaw depth does indicate that the permafrost table is closer to the surface, suggesting the vulnerability of the permafrost to surface disturbances.

Similar observations in Arctic Alaska have been given. Schaefer et al. (2015) proposed the Remotely Sensed Active Layer Thickness (ReSALT) algorithm to infer the ALT from the InSAR-based surface deformation signals on the assumption of volume contraction/expansion by phase change of pore ice/water. By critically examining whether ReSALT estimates were consistent with other ALT estimates by independent techniques such as ground-penetrating radar and probing, Schaefer et al. (2015) showed that the ReSALT estimates significantly overestimated ALT at drained thermokarst lake basins (DTLB) at Barrow, Alaska. Liu, Schaefer, et al. (2014) also showed anomalously large seasonal subsidence at DTLB at Prudhoe Bay, a nearby Arctic coastal plain and suggested the seasonal formation of excess ground ice.

The limitation of the Stefan function approach is also indicated by the ∼200% extended duration of uplift signals at the 2018 and 2019 scars in the year after the fire (Figures 3 and 5) and by the significant deepening of ALT (Figure 6). Even if the ADDF increased by a factor of 2, the corresponding freezing depth would increase at most by 140%; however, an observed increase in thaw depth by more than 200% at the 2018 scar suggests that additional process(es) are required to explain the observed increase in thaw depth. We interpret the prolonged uplift signals at scars firstly due to higher SWC originating in the reduced transpiration at the scar (Yoshikawa et al., 2003). Moreover, because the fires have burned off the surface organic mat, we can also expect decreased albedo and more significant absorption of solar radiation, leading to more efficient thawing of permafrost tables. At the burned area that lost the surface organic layer, we can further expect a greater temperature gradient between the surface and the permafrost table in winter, which is responsible for more significant thermomolecular pressure; a higher temperature gradient, however, causes a faster freezing rate and may reduce the heave rate (e.g., Rempel et al., 2004; Wettlaufer & Worster, 2006). The surface temperature in the burned area in winter is actually higher than that of the unburned site (Figure S7 in Supporting Information S1), which can be interpreted as due to the insulating effect of the possibly deeper snow cover in the burned area and/or the release of latent heat from the freezing SWC as reported in other cases (Smith et al., 2015; Worster & Wettlaufer, 1999; Yoshikawa et al., 2003). The temperature below the organic layer at the unburned site would presumably be higher than that at the burned area. However, we did not have such data because we set the thermometers above the organic layer in the unburned area and above the mineral layer in the burned area.

5.2. Post-Fire Transient Deformation: Concept Model

Liu et al. (2010, 2015) proposed a deformation model with a linear secular term plus a seasonally cyclic term for long-term permafrost degradation. However, post-fire deformation response at ice-rich permafrost would be more complex particularly during a transient phase. Indeed, our observations suggest that the seasonal freeze/thaw processes are no longer cyclic and that the secular term for the underlying permafrost thawing is neither linear. Instead, assuming that the linear secular term is negligibly small because of its slower effect than the

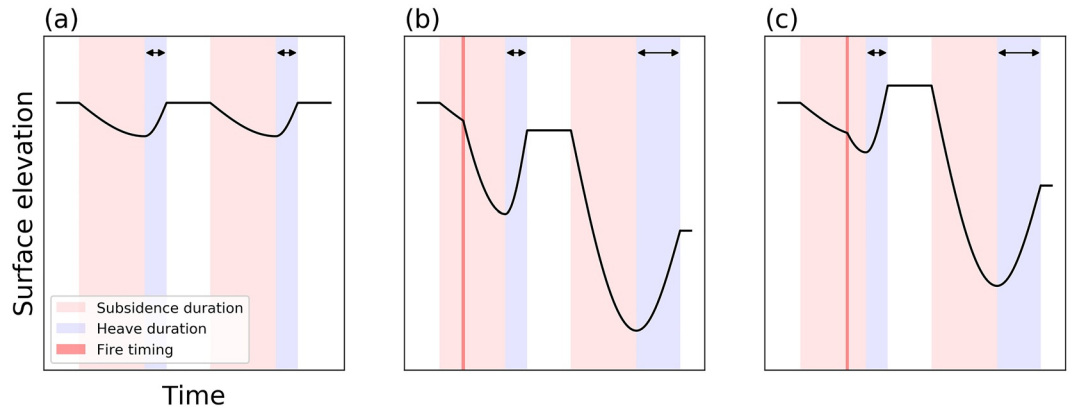

Figure 9. Conceptual image of transient freeze-thaw surface elevation response to fire during the first 2 years. (a) No fire. (b) Case of fire in the early thaw season, corresponding to the northern 2019 fire. (c) Case of fire in the late thaw season, corresponding to the 2018 and 2019 fires near BMS. In both (b) and (c), the heave duration is extended in the second year after fire. Both the post-fire subsidence and heave amplitude in (b) are larger than those in (c). It should be noted that a shallower (<60 cm) prefire ALT would be a prerequisite for significant post-fire subsidence, and that not all the burned areas will significantly subside.

post-fire abrupt impact on permafrost degradation, we consider that 1-year InSAR data during a transient phase is balanced by summer subsidence and (early-)winter heave. Here, the summer subsidence consists of prefire summer subsidence plus excess subsidence due to thawing of ice-rich permafrost (Figures 9b and 9c). In contrast, the winter heave consists of prefire winter heave plus excess heave caused by increased SWC and temperature gradient changes due to the removal of vegetation cover (Figures 9b and 9c). As prefire subsidence and prefire winter heave cancel each other (Figure 9a), the 1-year InSAR data during a transient phase is determined by the balance of excess subsidence, excess heave, and the timing of fire (Figures 9b and 9c).

The span-fire 1-year InSAR data indicate the net subsidence by as much as 13 cm at the 2019 scar to the north of Batagay (Figure 6), but the net uplift at the 2018 and 2019 scars near the BMS (Figures 4a and 4b). The two scars near the BMS started to show the net annual subsidence in the second year after the fire (Figures 4b and 4c). We interpret that two factors control these differences in their transient deformation response. The first important factor is the difference in when the fire occurred, which controls both the postfire ADDT and the enhanced SWC by reduced transpiration. For the 2019 scar to the north, there were 3 months available for the period of thawing, which can significantly deepen the thaw depth and reach the permafrost table, promoting the permafrost thawing and/or ground ice melting (Figure 9b). Moreover, the longer post-fire period will increase the SWC in the active layer via reduced transpiration and will enhance the frost-heave amplitude. In the case of the northern 2019 scar, the excess summer subsidence is larger than the excess winter heave (Figure 9b). On the other hand, for both 2018 and 2019 fires near BMS, the available periods for thaw depth deepening were 1 month and 2 months, respectively (Figure 9c). Nonetheless, the subsequent uplift exceeded the summer subsidence (Figures 4 and 9c and Figures S4 and S5 in Supporting Information S1), meaning that frost heave amplitude is not simply proportional to the thaw depth; this is also supported by the 2019 data in Figure 7b. Although the first post-fire heave amplitude in Figure 9c is smaller than that in Figure 9b, we interpret that the significant post-fire reduction in transpiration has enhanced the SWC in the active layer enough to make the excess heave greater than the excess subsidence (Figure 9c). Given the larger net annual subsidence at the 2018 scar near BMS (Figure 4) and the 2019 scar to the north (Figure 6), the second and probably more important factor in controlling the post-fire thermokarst subsidence is the original prefire ALT. At the 2019 scar to the north, the net annual subsidence signals are notably limited to a smaller portion of the entire burned area close to the 2014 scar (Figure 6). In light of the thaw depth data around the 2014 scar that could be used as a proxy for the 2019 scar to the north (Figure S3 in Supporting Information S1), they are relatively shallower (<60 cm) and similar to that at the 2018 unburned site (Figure 7a) than to the 2019 unburned site (Figure 7b). Comparing the 2018 scar with the adjacent 2019 scar, the cumulative subsidence at the 2018 scar was greater than that at the 2019 scar despite the shorter period available for thawing after the 2018 fire (Figure 4c). We can understand the difference due to the originally deeper thaw depth at the 2019 scar (Figure 7), and the shallower thaw depth at the 2018 scar was also evident from the diamond-shaped area.

Figure 10. Massive ground ice exposed at a new gully eroded adjacent to a man-made path, excavated to prevent the 2018 fire from expanding. Excavation, in combination with the presence of massive ice, seems to have accelerated significant erosion a couple of years after the 2018 fire. Photo was taken on 20 September 2021.

In contrast to the timing of fire, the duration of fire will not significantly affect the magnitude of excess subsidence. Considering that the 2018 and 2019 fires near BMS lasted 3 and 11 days, respectively, and the 2019 fire to the north lasted 12 days, the differences in the fire duration do not appear to impact the subsidence amplitude, whereas the duration of fire will control the burned area and also possibly the burn severity. If the fire duration is long, we may observe spatial heterogeneities in the subsidence amplitude because the burned area will include both deeper and shallower ALT areas.

All the fire scars show more significant annual subsidence in the first post-fire year than in the span-fire year (Figures 4 and 6), indicating the dominance of excess subsidence over excess heave in the post-fire year (Figure 9). This is consistent with the deeper thaw depth in the second year after fire (Figure 7) because the loss of the surface organic layer is responsible for reduced albedo, transpiration, and subsequent higher SWC that further increases the thermal conductivity (Yoshikawa et al., 2003). Moreover, the fire scars show increased heave amount and extended heave duration from the first to the second year (Figures 3, 5, 9b, and 9c). The post-fire excess frost heave is firstly due to the significant reduction in the transpiration by the loss of surface vegetation and the subsequent increase in SWC in the active layer. In addition, this would be due to the undrained SWC in the second year, which will be more significant where the prefire ALT is shallow.

There is one more lesson from the diamond-shaped area where the controlled site for the 2018 fire is located. Because of the shallower thaw depth than the other control sites, seasonal subsidence and heave amplitude are larger. However, there is no net annual subsidence. We interpret that the organic layer (Figure 8) prevents the area from undergoing net annual subsidence, playing a crucial role as a thermal insulator (Yoshikawa et al., 2003). After the former surface disturbance, the diamond-shaped area seems to be currently in stable condition with higher SWC than other areas.

5.3. Possibility of Another Megaslump Formation

Comparing the subsidence signals in this study with those at the 2014 scar reported by Yanagiya and Furuya (2020), it turns out that the cumulative subsidence at the 2014 scar until the following year after the fire was more significant than those at the 2018 and 2019 scars near BMS by more than ∼5 cm. Furthermore, the subsidence amplitude at the 2019 scar to the north seems comparable to that at the 2014 scar, but the subsiding area is restricted to the western region. These observations suggest that the 2014 scar was either much richer in ground ice content or underlain by a shallower permafrost table than the area around the 2018 and 2019 scars near the BMS. However, the rapid subsidence rate during 2015–2016 at the 2014 scar (Yanagiya & Furuya, 2020) already slowed down in 2019 (Figure 6), probably because no further ALT deepening is possible beyond the ALT of 124 ± 17 cm as of September 2019 (Figure S3 in Supporting Information S1). Thus, it seems unlikely that another megaslump can develop at the 2014 scar.

In light of the smaller cumulative subsidence signals at the 2018 and 2019 scars near the BMS, it might also appear unlikely to form another megaslump. However, we cannot rule out its possibility. At the time of onsite observation in 2021, we noticed that an artificial path excavated to prevent the 2018 fire from further expanding underwent significant erosion. Moreover, the water flow from the artificial path generated a new gully in an unburned area adjacent to the 2018 scar, where massive ground ice was exposed in the air (Figure 10). These are not the consequences from surface subsidence but from erosion, which cannot be resolved by InSAR because of coherence loss. Namely, the artificial fire-prevention path could likely promote further erosion and trigger another thaw slump. Therefore, we need to monitor and, if necessary, perform some engineering protections. In view of the proximity of the diamond-shaped area to the BMS (Figure 1b), it is likely that either ice-rich permafrost or shallower permafrost-table or both are continuously distributed in the nearby area. It is uncertain, however, why the top of the massive ice layer is at such shallower depth near Batagay.

Notably, the maximum ALTs of 120–130 cm could be derived commonly from 2014, 2018, and 2019 scars, despite their different cumulative subsidence amplitudes. Therefore, we may interpret that the maximum ALT is

limited to the depth at which atmospheric heat transfer is possible near Batagay. It is deferred for future studies to examine if and how the permafrost aggradation and subsequent ALT shallowing will occur in combination with surface vegetations' recovery.

6. Conclusions

We examined transient freeze-thaw deformation responses to the 2018 and two 2019 fires near Batagay, Northeast Siberia, by detecting span-fire and post-fire deformation with two independent InSAR images and performing onsite thaw depth measurements at the 2018 and 2019 scars near the BMS. Besides the fire scars, we also detected clear seasonal uplift without net annual subsidence in a specific area near the 2018 scar. Both InSAR and thaw depth data revealed diverse post-fire responses regarding the timing of subsidence initiation, location, and amplitude. Comparing the span-fire and post-fire deformation signals around the fire scars near Batagay, we demonstrated that, once the surface organic layers are burned, the transient freeze-thaw responses to fires were controlled by the original depth to the permafrost table as well as the timing of fires.

Data Availability Statement

ALOS-2/PALSAR-2 level 1.1 data can be searched and purchased from either PASCO (http://en.alos-pasco.com) or RESTEC (https://www.restec.or.jp/en/), which are the authorized data providers from JAXA. ALOS-2/PALSAR-2 level 1.1 data are also available if your research proposal for Earth observation using satellite images is accepted through reviewing processes, although the announcement is launched irregularly (https://www.eorc.jaxa.jp/ALOS/en/index_e.htm). Sentinel-1 SLC and Sentinel-2 optical data are freely available via the Copernicus Open Access Hub (https://scihub.copernicus.eu/dhus/#/home). ArcticDEM datasets are available from the Polar Geospatial Center (PGC) website (https://www.pgc.umn.edu/data/arcticdem/). Temperature and thaw depth data are archived at the Zenodo repository (https://doi.org/10.5281/zenodo.6782395). GAMMA software was developed by Gamma Remote Sensing (https://www.gamma-rs.ch). The Scientific color maps "roma" and "batlow" (Crameri, 2021) are used in the InSAR and coherence images, respectively.

Acknowledgments
We acknowledge Dr. Lin Liu and two anonymous reviewers, whose detailed comments were helpful to improve the original manuscript. This study was supported by KAKENHI (18H03353 and 19K03982) from the Japan Society for the Promotion of Science and Joint Research Programs of Japan Arctic Research Network Center from 2017 to 2021 (Suishin14, 01, 09, 06, 10, and FS04). In addition, KY acknowledges support for travel fees of field observation from the Overseas Fellowship Program, Arctic Challenge for Sustainability II (ArCS II) Project. GI acknowledges support from the Belmont Forum Collaborative Research (NSF Grant #2129253). We thank Dr. Alexander Fedorov, Mr. Nikolai Fedorov, and other scientists of Melnikov Permafrost Institute for the invitation and cooperation in the field observations. PALSAR-2 level 1.1 data are shared with the PALSAR Interferometry Consortium Study our Evolving Land Surface (PIXEL) under a cooperative research contract with the Earthquake Research Institute, University of Tokyo. The ownership of ALOS-2/PALSAR-2 data belongs to JAXA.

References

Bürgmann, R., Rosen, P. A., & Fielding, E. J. (2000). Synthetic aperture radar interferometry to measure Earth's surface topography and its deformation. *Annual Review of Earth and Planetary Sciences*, *28*(1), 169–209. https://doi.org/10.1146/annurev.earth.28.1.169

Crameri, F. (2021). Scientific colour maps (version 7.0.1) [Dataset]. Zenodo. https://doi.org/10.5281/zenodo.5501399

Frost, G. V., Loehman, R. A., Saperstein, L. B., Macander, M. J., Nelson, P. R., Paradis, D. P., & Natalli, S. M. (2020). Multi-decadal patterns of vegetation succession after tundra fire on the Yukon-Kuskokwim Delta, Alaska. *Environmental Research Letters*, *15*(2), 025003. https://doi.org/10.1088/1748-9326/ab5f49

Gillett, N. P., Weaver, A. J., Zwiers, F. W., & Flannigan, M. D. (2004). Detecting the effect of climate change on Canadian forest fires. *Geophysical Research Letters*, *31*(18), L18211. https://doi.org/10.1029/2004GL020876

Goldstein, R. M. (1995). Atmospheric limitations to repeat-track radar interferometry. *Geophysical Research Letters*, *22*(18), 2517–2520. https://doi.org/10.1029/95gl02475

Gomba, G., Parizzi, A., Zan, F. D., Eineder, M., & Bamler, R. (2016). Toward operational compensation of ionospheric effects in SAR interferograms: The split-spectrum method. *IEEE Transactions on Geoscience and Remote Sensing*, *54*(3), 1446–1461. https://doi.org/10.1109/TGRS.2015.2481079

Gruber, S. (2020). Ground subsidence and heave over permafrost: Hourly time series reveal interannual, seasonal and shorter-term movement caused by freezing, thawing and water movement. *The Cryosphere*, *14*(4), 1437–1447. https://doi.org/10.5194/tc-14-1437-2020

Guneriussen, T., Høgda, K. A., Johnsen, H., & Lauknes, I. (2001). InSAR for estimation of changes in snow water equivalent of dry snow. *IEEE Transactions on Geoscience and Remote Sensing*, *39*(10), 2101–2108. https://doi.org/10.1109/36.957273

Hanssen, R. F. (2001). *Radar interferometry: Data interpretation and error analysis, Kluwer*. Academic Publishers.

Holloway, J. E., Lewkowicz, A. G., Douglas, T. A., Li, X., Turetsky, M. R., Baltzer, J. L., & Jin, H. (2020). Impact of wildfire on permafrost landscapes: A review of recent advances and future prospects. *Permafrost and Periglacial Processes*, *31*(3), 371–382. https://doi.org/10.1002/ppp.2048

Hu, Y., Liu, L., Larson, K. M., Schaefer, K. M., Zhang, J., & Yao, Y. (2018). GPS interferometric reflectometry reveals cyclic elevation changes in thaw and freezing seasons in a permafrost area (Barrow, Alaska). *Geophysical Research Letters*, *45*(11), 5581–5589. https://doi.org/10.1029/2018GL077960

Iwahana, G., Uchida, M., Liu, L., Gong, W., Meyer, F. J., Guritz, R., et al. (2016). InSAR detection and field evidence for thermokarst after a tundra wildfire, using ALOS-PALSAR. *Remote Sensing*, *8*(3), 218. https://doi.org/10.3390/rs8030218

Jorgenson, M. (2013). Thermokarst terrains. In J. Shroder, R. Giardino, & J. Harbor (Eds.), *Treatise on Geomorphology*, *Glacial and periglacial geomorphology* (Vol. 8, pp. 313–324). Academic Press.

Kasischke, E. S., Verbyla, D. L., Rupp, T. S., Mcguire, A. D., Murphy, K. A., Jandt, R., et al. (2010). Alaska's changing fire regime—Implications for the vulnerability of its boreal forests. *Canadian Journal of Forest Research*, *40*(7), 1313–1324. https://doi.org/10.1139/x10-098

Kizyakov, A. I., Wetterich, S., Günther, F., Opel, T., Jongejans, L. L., Courtin, J., et al. (2023). Landforms and degradation pattern of the Batagay thaw slump, Northeastern Siberia. *Geomorphology*, *420*, 108501. https://doi.org/10.1016/j.geomorph.2022.108501

Klene, A. E., Nelson, F. E., Shiklomanov, N. I., & Hinkel, K. M. (2001). The N-factor in natural landscapes: Variability of air and soil-surface temperatures, Kuparuk River Basin, Alaska, USA. *Arctic, Antarctic, and Alpine Research*, *33*(2), 140–148. https://doi.org/10.2307/1552214
Kokelj, S. V., & Jorgenson, M. T. (2013). Advances in thermokarst research. *Permafrost and Periglacial Processes*, 24(2), 108–119. https://doi.org/10.1002/ppp.1779
Kunitsky, V. V., Syromyatnikov, I. I., Schirrmeister, L., Skachov, Y. B., Grosse, G., Wetterich, S., & Grigoriev, M. N. (2013). Ice-rich permafrost and thermal denudation in the Batagay area (Yana Upland, East Siberia). *Earth Cryosphere (Kriosfera Zemli)*, *17*(1), 56–68. (in Russian).
Liu, L., Jafarov, E. E., Schaefer, K. M., Jones, B. M., Zebker, H. A., Williams, C. A., et al. (2014). InSAR detects increase in surface subsidence caused by an Arctic tundra fire. *Geophysical Research Letters*, *41*(11), 3906–3913. https://doi.org/10.1002/2014GL060533
Liu, L., Schaefer, K., Gusmeroli, A., Grosse, G., Jones, B. M., Zhang, T., et al. (2014). Seasonal thaw settlement at drained thermokarst lake basins, Arctic Alaska. *The Cryosphere*, *8*(3), 815–826. https://doi.org/10.5194/tc-8-815-2014
Liu, L., Schaefer, K., Zhang, T., & Wahr, J. (2012). Estimating 1992–2000 average active layer thickness on the Alaskan North Slope from remotely sensed surface subsidence. *Journal of Geophysical Research*, *117*(F1), F01005. https://doi.org/10.1029/2011JF002041
Liu, L., Schaefer, K. M., Chen, A. C., Gusmeroli, A., Zebker, H. A., & Zhang, T. (2015). Remote sensing measurements of thermokarst subsidence using InSAR. *Journal of Geophysical Research: Earth Surface*, *120*(9), 1935–1948. https://doi.org/10.1002/2015JF003599
Liu, L., Zhang, T., & Wahr, J. (2010). InSAR measurements of surface deformation over permafrost on the North Slope of Alaska. *Journal of Geophysical Research: Earth Surface*, *115*(3), F03023. https://doi.org/10.1029/2009JF001547
Massonnet, D., & Feigl, K. L. (1998). Radar interferometry and its application to changes in the Earth's surface. *Reviews of Geophysics*, *36*(4), 441–500. https://doi.org/10.1029/97RG03139
McCarty, J. L., Aalto, J., Paunu, V.-V., Arnold, S. R., Eckhardt, S., Klimont, Z., et al. (2021). Reviews and syntheses: Arctic fire regimes and emissions in the 21st century. *Biogeosciences*, *18*, 5053–5083. https://doi.org/10.5194/bg-18-5053-2021
Michaelides, R. J., Zebker, H. A., Schaefer, K., Parsekian, A., Liu, L., Chen, J., et al. (2019). Inference of the impact of wildfire on permafrost and active layer thickness in a discontinuous permafrost region using the remotely sensed active layer thickness (ReSALT) algorithm. *Environmental Research Letters*, *14*(3), 035007. https://doi.org/10.1088/1748-9326/aaf932
Molan, Y. E., Kim, J. W., Lu, Z., Wylie, B., & Zhu, Z. (2018). Modeling wildfire-induced permafrost deformation in an Alaskan boreal forest using InSAR observations. *Remote Sensing*, *10*(3), 405. https://doi.org/10.3390/rs10030405
Murton, J. B., Opel, T., Toms, P., Blinov, A., Fuchs, M., Wood, J., et al. (2022). A multimethod dating study of ancient permafrost, Batagay megaslump, East Siberia. *Quaternary Research*, *105*, 1–22. https://doi.org/10.1017/qua.2021.27
Nelson, F. E., Shiklomanov, N. I., Mueller, G. R., Hinkel, K. M., Walker, D. A., & Bockheim, J. G. (1997). Estimating active-layer thickness over a large region: Kuparuk River Basin, Alaska, USA. *Arctic & Alpine Research*, *29*(4), 367. https://doi.org/10.2307/1551985
Ponomarev, E., Kharuk, V., & Ranson, K. (2016). Wildfires dynamics in Siberian larch forests. *Forests*, *7*(12), 125. https://doi.org/10.3390/f7060125
Porter, C., Morin, P., Howat, I., Noh, M., Bates, B., Peterman, K., et al. (2018). ArcticDEM. *Harvard Dataverse, V1*. [2021.7.14]. https://doi.org/10.7910/DVN/OHHUKH
Rempel, A. W., Wettlaufer, J. S., & Worster, M. G. (2004). Premelting dynamics in a continuum model of frost heave. *Journal of Fluid Mechanics*, *498*, 227–224. https://doi.org/10.1017/S0022112003006761
Rignot, E., Echelmeyer, K., & Krabill, W. (2001). Penetration depth of interferometric synthetic-aperture radar signals in snow and ice. *Geophysical Research Letters*, *28*(18), 3501–3504. https://doi.org/10.1029/2000GL012484
Schaefer, K., Liu, L., Parsekian, A., Jafarov, E., Chen, A., Zhang, T., et al. (2015). Remotely sensed active layer thickness (ReSALT) at Barrow, Alaska using interferometric synthetic aperture radar. *Remote Sensing*, *7*(4), 3735–3759. https://doi.org/10.3390/rs70403735
Schuur, E. A. G., McGuire, A. D., Schädel, C., Grosse, G., Harden, J. W., Hayes, D. J., et al. (2015). Climate change and the permafrost carbon feedback. *Nature*, *520*(7546), 171–179. https://doi.org/10.1038/nature14338
Shiklomanov, N. I., Streletskiy, D. A., Little, J. D., & Nelson, F. E. (2013). Isotropic thaw subsidence in undisturbed permafrost landscapes. *Geophysical Research Letters*, *40*(24), 6356–6361. https://doi.org/10.1002/2013GL058295
Shur, Y., Hinkel, K. M., & Nelson, F. E. (2005). The transient layer: Implication for geocryology and climate-change science. *Permafrost and Periglacial Processes*, *16*(1), 5–17. https://doi.org/10.1002/ppp.518
Simons, M., & Rosen, P. A. (2015). Interferometric synthetic aperture radar geodesy. In *Treatise on Geophysics* (2nd ed., Vol. 3). Elsevier B.V. https://doi.org/10.1016/B978-0-444-53802-4.00061-0
Smith, S. L., Riseborough, D. W., & Bonnaventure, P. P. (2015). Eighteen year record of forest fire effects on ground thermal regimes and permafrost in the central Mackenzie valley, NWT, Canada. *Permafrost and Periglacial Processes*, *26*(4), 289–303. https://doi.org/10.1002/ppp.1849
Taber, S. (1929). Frost heaving. *The Journal of Geology*, *37*(5), 428–461. https://doi.org/10.1086/623637
Taber, S. (1930). The mechanics of frost heaving. *The Journal of Geology*, *38*(4), 303–317. https://doi.org/10.1086/623720
Tarnocai, C., Canadell, J. G., Schuur, E. A. G., Kuhry, P., Mazhitova, G., & Zimov, S. (2009). Soil organic carbon pools in the northern circumpolar permafrost region. *Global Biogeochemical Cycles*, *23*(2), GB2023. https://doi.org/10.1029/2008gb003327
Tsai, Y. L. S., Dietz, A., Oppelt, N., & Kuenzer, C. (2019). Remote sensing of snow cover using spaceborne SAR: A review. *Remote Sensing*, *11*(12), 1456. https://doi.org/10.3390/rs11121456
Turetsky, M. R., Abbott, B. W., Jones, M. C., Anthony, K. W., Olefeldt, D., Schuur, E. A. G., et al. (2020). Carbon release through abrupt permafrost thaw. *Nature Geoscience*, *13*(2), 138–143. https://doi.org/10.1038/s41561-019-0526-0
Wegmüller, U., & Werner, C. L. (1997). Gamma SAR processor and interferometry software. In *Proceedings of the 3rd ERS Symposium* (pp. 1687–1692). European Space Agency Special Publication, ESA SP-414.
Wettlaufer, J. S., & Worster, M. G. (2006). Premelting dynamics. *Annual Review of Fluid Mechanics*, *38*(1), 427–452. https://doi.org/10.1146/annurev.fluid.37.061903.175758
Worster, M. G., & Wettlaufer, J. S. (1999). The fluid mechanics of premelted liquid films. In W. Shyy & R. Narayanan (Eds.), *Fluid dynamics at interfaces* (pp. 339–351). Cambridge University Press.
Yanagiya, K., & Furuya, M. (2020). Post-wildfire surface deformation near Batagay, eastern Siberia, detected by L-band and C-band InSAR. *Journal of Geophysical Research: Earth Surface*, *125*(7), e2019JF005473. https://doi.org/10.1029/2019jf005473
Yoshikawa, K., Bolton, W. R., Romanovsky, V. E., Fukuda, M., & Hinzman, L. D. (2003). Impacts of wildfire on the permafrost in the boreal forests of Interior Alaska. *Journal of Geophysical Research*, *107*(D1), 8148. https://doi.org/10.1029/2001JD000438
Zhang, Y., Wolfe, S. A., Morse, P. D., Fraser, I. O. R. H., & Fraser, R. H. (2015). Spatiotemporal impacts of wildfire and climate warming on permafrost across a subarctic region, Canada. *Journal of Geophysical Research: Earth Surface*, *120*(11), 2338–2356. https://doi.org/10.1002/2015JF003679

References From the Supporting Information

Burn, C. R. (1998). The response (1958–1997) of permafrost and near-surface ground temperatures to forest fire, Takhini River valley, southern Yukon Territory. *Canadian Journal of Earth Sciences*, *35*(2), 184–199. https://doi.org/10.1139/e97-105

Key, C. H., & Benson, N. C. (2006). Landscape Assessment (LA) sampling and analysis methods. *USDA Forest Service - General Technical Report RMRS-GTR, 164 RMRS-GTR*.

Zhong, X., Zhang, T., & Wang, K. (2014). Snow density climatology across the former USSR. *The Cryosphere*, *8*(2), 785–799. https://doi.org/10.5194/tc-8-785-2014